Nanoscale

Volume 1 | Number 1 | Jan 2013 | Pages 1–100

Nanoscale

www.rsc.org/nanoscale

ROYAL SOCIETY OF CHEMISTRY

ROYAL SOCIETY OF CHEMISTRY

www.rsc.org/nanoscale

Nanoscale

An inorganic capping strategy for the seeded growth of versatile bimetallic nanostructures

Yuchen Pei, Raghu V. Maligal–Ganesh, Chaoxian Xiao, Tian–Wei Goh, Kyle Brashler, Jeffrey A. Gustafson and Wenyu Huang [a]

Metal nanostructures have attracted great attention in various fields due to their tunable properties through precisely tailored sizes, compositions and structures. Using mesoporous silica (mSiO₂) as the inorganic capping and encapsulated Pt nanoparticles as the seeds, we developed a robust seeded growth method to prepare uniform bimetallic nanoparticles encapsulated in mesoporous silica shells (PtM@mSiO₂, M = Pd, Rh, Ni and Cu). Unexpectedly, we found that the inorganic silica shell is able to accommodate an eight–fold volume increase in the metallic core by reducing its thickness. The bimetallic nanoparticles encapsulated in mesoporous silica shells showed enhanced catalytic properties and thermal stabilities compared with those prepared with organic capping agents. This inorganic capping strategy could find a broad application in the synthesis of versatile bimetallic nanostructures with exceptional structural control and enhanced catalytic properties.

Introduction

Uniform and tunable metal nanostructures have been extensively investigated as advanced materials in imaging, drug delivery, and heterogeneous catalysis.[1-3] Among them, bimetallic nanoparticles (NPs) have been attractive paradigms to study their tunable electronic and chemical properties resulting from synthetic advances that enable size, composition and morphology control.[4-17] Seeded growth approaches[18] are commonly applied in colloidal chemistry to synthesize diverse bimetallic nanostructures such as core–shell, alloy, and hollow structures in a predictable and controllable manner.[8,9,19] In general colloidal synthesis, organic surfactants are indispensable to prevent the aggregation of NPs, functioning as capping agents.[20-22] However, NPs capped with organic surfactants would aggregate under harsh reaction or pretreatment conditions.[21] Moreover, organic capping agents can stymie the access of reactants to the surface of NPs, and thus limit their catalytic performance.[23] Thermal treatment can remove organic capping agents, but usually leads to undesired aggregation of the NPs. To enhance the stability of NPs, oxides and carbon materials (e.g. Al₂O₃, SiO₂, and functionalized graphene) have been used as supports to immobilize them.[24-26] Unfortunately, the sintering of supported NPs is still unavoidable under high temperature treatments.[27] To further enhance the thermal stability of NPs, another strategy is to encapsulate them within inorganic shells, such as mesoporous silica (mSiO₂), which can provide a robust three–dimensional protection against NP sintering.[28-42]
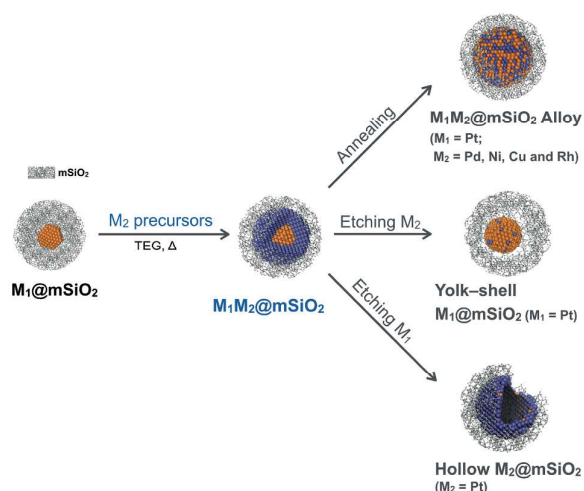
In the synthesis of bimetallic@mSiO₂ core–shell NPs, the traditional strategy relies on the pre–synthesis of bimetallic NPs followed by coating mSiO₂,[43,44] where organic capping agents still play key roles in the synthesis of bimetallic NPs, resulting in the challenging removal of organic surfactants bound to the surface of the bimetallic NPs. Inspired by the structural similarities between NPs capped with organic surfactants and inorganic shells, we hypothesized that the inorganic shell can be directly used as a stabilizer or "capping agent" for the growth of uniform bimetallic NPs from monometallic NP seeds encapsulated within this inorganic shell.

We explored this inorganic stabilizer concept for the first time using mSiO₂ as a robust inorganic shell for the synthesis of various Pt–based bimetallic@mSiO₂ NPs (PtM@mSiO₂). Pt NPs encapsulated in mSiO₂ shells (Pt@mSiO₂) were used as seeds where mSiO₂ functioned as an inorganic "capping agent". We then introduced a secondary metal (Pd, Rh, Ni, or Cu) onto Pt@mSiO₂ via seeded growth as illustrated by the first step in Scheme 1. The increase in the metal core volume due to the deposition of secondary metals is accommodated by the decrease in the mSiO₂ shell thickness. This suggests that the mSiO₂ shell is not a rigid coating and can be easily deformed to accommodate the expansion of the encapsulated metal core during the seeded growth. We demonstrated that four different nanostructures could be easily synthesized using this inorganic capping strategy. Initially, the deposited secondary metal forms a shell in between the original metal core and the deformed mSiO₂ shell under the employed synthesis conditions. Upon further annealing, the bimetallic core could be converted to an alloy. We could also selectively etch away the original metal core or the secondary metal shell leading to a mSiO₂–encapsulated nanobox or yolk–shell structure, respectively. Moreover, the mSiO₂ shell permits the access of reactants to the clean metal surface after bimetallic seeded growth in the absence of strong organic capping agents. We found that PtPd bimetallic NPs capped with mSiO₂ shells showed superior catalytic properties compared to those capped with organic capping agents.

a. Ames Laboratory, U.S. Department of Energy
   Department of Chemistry, Iowa State University, Ames, 50011, USA
   E-mail: whuang@iastate.edu

Scheme 1. Seeded growth of bimetallic $M_1M_2@mSiO_2$ NPs from $M_1@mSiO_2$ seeds and their derived nanostructures.

Experimental

Synthesis of bimetallic PtPd@mSiO_2 NPs. In a typical synthesis of PtPd@mSiO_2 NPs, as–synthesized Pt@mSiO_2 seeds (10 mg Pt, stored in methanol) and K_2PdCl_4 (16.7 mg, as Pt/Pd=1) precursor were well dispersed in 80 mL TEG with sonication. The mixed solution was placed in vacuum to remove residual methanol, after which argon was backfilled into the flask. Under argon protection, the mixture was heated at 180 ˚C for 2 hrs (ramping rate: 2.5 ˚C·min^{-1}) from 30 ˚C and subsequently heated at 280 ˚C for another 2 hrs (ramping rate: 1.7 ˚C·min^{-1}) with vigorous stirring. After cooling down to room temperature, 80 mL of acetone was added into the solution to help separate PtPd@mSiO_2 NPs. PtPd@mSiO_2 NPs were then collected by centrifuge and further washed with methanol three times. As–synthesized PtPd@mSiO_2 NPs were stored in methanol for future use.

Yolk–shell Pt@mSiO_2 and hollow Pt@mSiO_2 nanoboxes. Yolk–shell and hollow Pt@mSiO_2 were derived from their respective PtPd bimetallic nanostructures by preferential etching of Pd by HNO_3. Yolk–shell Pt@mSiO_2 was obtained by placing 0.5 mg PtPd@mSiO_2 powder (Pt core/Pd shell) in 5 mL concentrated HNO_3 and stirring for 18 hrs at room temperature. Before HNO_3 etching, PtPd@mSiO_2 samples were pre–dried in vacuum at room temperature and further dried at 120 ˚C in an oven overnight. Hollow Pt@mSiO_2 was obtained by placing 2 mg PdPt@mSiO_2 (Pt shell/Pd core) in 10 mL concentrated HNO_3 under reflux for 18 hrs.

Control experiment for mSiO_2 etching. TEG blank (control i) was conducted using Pt@mSiO_2 (10 mg Pt) directly in 80 mL TEG under the same temperature ramping conditions as that for the synthesis of PtPd@mSiO_2. KCl treatment (control ii) was conducted using Pt@mSiO_2 (10 mg Pt) in 80 mL TEG with the addition of four molar equivalents of KCl (comparing to Pt).

Characterization. Surface analysis of Pt@mSiO_2 and PtPd_{1.1}@mSiO_2 was performed by nitrogen adsorption isotherms using Micromeritics 3Flex surface characterization analyzer at 77 K. PXRD patterns of the samples were acquired by a STOE Stadi P powder diffractometer using Cu Kα radiation (40 kV, 40 mA, λ = 0.1541 nm).

TEM, EDS line scans and elemental mapping analysis for the morphology of Pt@mSiO_2, Pd@mSiO_2 and PtM@mSiO_2 were investigated using TEM recorded on a Tecnai G2 F20 electron microscope with EDS analysis (Oxford INCA EDS) operated at 200 kV. ICP–MS (X Series II, Thermo Scientific) was performed to determine the actual metal loadings of Pt@mSiO_2 and Pd@mSiO_2 ahead of the introduction of the secondary metal precursor, and to determine metal ratios of PtM@mSiO_2 after synthesis. Samples were first dissolved in a mixture of 100 μL HF and 5 mL aqua regia to dissolve the mSiO_2 shell for efficient digestion of metals. After evaporating the solution containing HF under 250 ˚C, the remaining solids were further dissolved in 5 mL aqua regia to achieve a clear solution with metal ions, and diluted appropriately for ICP–MS detection.

Nitrobenzene hydrogenation. PtPd@mSiO_2 catalysts were collected from their methanol suspension solution and then dried under vacuum. The compositions of Pt and Pd of catalysts were measured by ICP–MS. The catalysts were calcined at 350 ˚C in air for 4 hrs and reduced at 300 ˚C for 2 hrs in 5 % H_2/He flow before reaction. Typically, calculated amounts of dried catalyst powder ($2.6×10^{-3}$ mmol Pt + Pd) were weighed in a 20 mL glass vial, followed by the addition of 410 μL nitrobenzene, 1.5 mL H_2O and 300 μL ethylene glycol as the internal standard. The vial was then sealed with a rubber cap equipped with a needle to aid H_2 diffusion. Then 2 or 3 vials were placed inside a Parr autoclave charged with 4 MPa H_2 after suction and flushing was carried out several times. The reaction was conducted under room temperature (~ 25 ˚C) with vigorous stirring. All contents (nitrobenzene, nitrosobenzene, phenylhydroxylamine, aniline, and azoxybenzene) after reaction were analyzed directly by an Agilent 6890N/5975 gas chromatograph mass spectroscopy (GS–MS) equipped with a HP–5ms capillary column (30 m × 0.25 mm × 0.25 μm) and a flame ionization detector.

Results and discussion

Pt NPs encapsulated in mSiO_2 shells (Pt@mSiO_2) were prepared as reported earlier.[42] To form PtM@mSiO_2 (M = Pd, Rh, Ni, Cu) bimetallic NPs, Pt@mSiO_2 seeds and a secondary metal precursor were dispersed and reduced in tetraethylene glycol (TEG) at elevated temperatures under argon atmosphere (Scheme 1).[45] To avoid the formation of isolated NPs by the fast nucleation of the secondary metal precursor, we adjusted the reduction temperature for different metal precursors. For 3d metal precursors ($NiCl_2$ and $CuCl_2$), the reduction temperature was kept at 280 ˚C, while 180 ˚C was used to reduce noble metal precursors (K_2PdCl_4 and $RhCl_3$). At the appropriate reduction temperature, the secondary metal prefers to deposit on the Pt core encapsulated in mSiO_2 due to the relatively lower nucleation energy barrier required for seeded growth as opposed to forming independent nuclei.[46] Pt NPs can also catalyze the dehydrogenation of TEG,[47-49] generating hydrogen species on the surface of Pt that could localize the reduction and thus the selective deposition of the secondary metal.

Prior to the synthesis of bimetallic PtM@mSiO_2 NPs from Pt@mSiO_2 seeds, we were wondering if the limited space within the mSiO_2 shell would restrict the growth of bimetallic NPs from Pt cores. We first performed the seeded growth with K_2PdCl_4 precursor and Pt@mSiO_2 seeds. After reduction at 180 ˚C for 2 hrs, the overall particle size (including the mSiO_2 shell) and the mSiO_2 shell morphology of final PtPd_{1.1}@mSiO_2 NPs (overall size: 36.3 ± 1.9 nm) show no obvious change compared with those of

Pt@mSiO$_2$ seeds (overall size: 36.1 ± 1.8 nm), though the metal core expands to 17.7 ± 1.2 nm from 13.6 ± 1.0 nm as shown by the transmission electron microscopy (TEM) images in Figure 1a and 1b. To accommodate the metal core expansion, the thickness of the mSiO$_2$ shell decreases to 9.3 ± 1.1 nm from 11.3 ± 1.1 nm. We speculate that the mSiO$_2$ shell is either etched or compressed specifically from the inner surface. Specific surface areas and pore volumes of Pt@mSiO$_2$ and PtPd$_{1.1}$@mSiO$_2$ are shown in Table S1 and Figure S1 in the Supporting Information measured by N$_2$ physisorption. The specific surface area and pore volume of PtPd$_{1.1}$@mSiO$_2$ decrease accompanied by a slight increase in pore size, compared with those of Pt@mSiO$_2$. Considering the unchanged sizes of the overall particles, decreased surface areas, and nearly intact pore sizes, we suggest the loss of mSiO$_2$ during seeded growth of PtPd@mSiO$_2$, likely etched by ions in TEG during synthesis. It has been reported that inorganic ions can etch amorphous silica.[50]
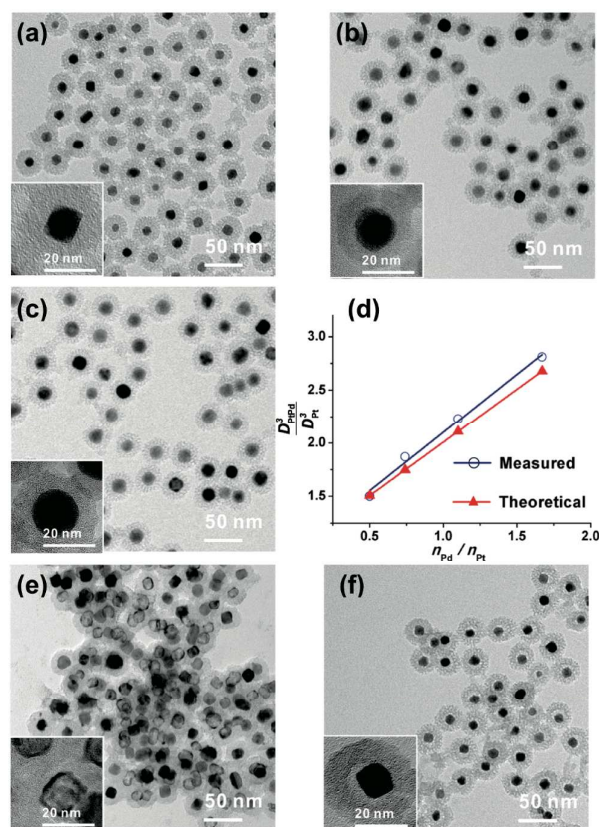

Figure 1. TEM images showing the morphology of (a) Pt@mSiO$_2$; (b) PtPd$_{1.1}$@mSiO$_2$; (c) PtPd$_{1.6}$@mSiO$_2$; (d) Linear relationship between volumetric ratios of PtPd/Pt metal core and Pd/Pt molar ratios; (e) hollow Pt nanobox@mSiO$_2$ from PdPt$_{0.48}$@mSiO$_2$ after etching Pd by HNO$_3$; (f) yolk–shell Pt@mSiO$_2$ by etching Pd in PtPd@mSiO$_2$.

To illustrate the etching of the mSiO$_2$ shell by ions, we conducted two control experiments under the same synthesis conditions: (i) Pt@mSiO$_2$ seeds were heated in TEG; (ii) KCl was added to hot TEG that contained Pt@SiO$_2$ seeds. In the first control experiment (Figure S2a and S2b), we found that the overall size of Pt@mSiO$_2$ is ~ 35 nm and the Pt core is ~ 13 nm, which conforms to that of the

original Pt@mSiO$_2$ (overall size: 36.1 ± 1.8 and Pt core: 13.6 ± 1.0 nm). The specific area of Pt@mSiO$_2$ in control (i) is 594.8 cm^2·g^{-1} with a pore size of 2.5 nm. This is also similar to that of the original Pt@mSiO$_2$ (specific area: 503.4 cm^2·g^{-1} and pore size: 2.4 nm). This blank control serves to show the mSiO$_2$ shell is stable without obvious deformation in TEG during our seeded growth. In the second control experiment, 4 equivalents of KCl were added to the hot TEG solution that contained Pt@mSiO$_2$ to study the capacity of KCl to etch mSiO$_2$ under our synthesis conditions. The amount of KCl is comparable to the added K$_2$PdCl$_4$ precursor in a typical synthesis. The diameter of Pt core and overall size (including the mSiO$_2$ shell) in Pt@mSiO$_2$–KCl (control ii) are 13.3 ± 0.8 nm and 31.3 ± 1.7 nm respectively. The 5 nm decrease in overall size of Pt@mSiO$_2$–KCl and the relatively intact Pt core size suggests the etching of the mSiO$_2$ shell in presence of KCl. We also used N$_2$ adsorption to characterize Pt@mSiO$_2$–KCl control. Due to etching by the KCl, the specific area of Pt@mSiO$_2$–KCl decreased to 442.0 cm^2·g^{-1} from 503.4 cm^2·g^{-1} in the original Pt@mSiO$_2$. Pore size distribution of Pt@mSiO$_2$–KCl in Figure S2d also shows a bump at 4.9 nm besides the peak at 2.6 nm, which indicates that the well–defined pore structure of mSiO$_2$ was partially destroyed in presence of KCl. The etching of mSiO$_2$ was also supported by the increase of Si content in the supernatant of the solution after synthesis (Table S2). We speculate that the localized production of ions during the reduction of metal precursors (e.g. H$^+$, K$^+$ and Cl$^-$ in the case of K$_2$PdCl$_4$) would occur predominantly at the inner surface of mSiO$_2$, near the metal NP cores, where Pd is being nucleated on the surface of Pt NPs during seeded growth. The heat of the reaction and/or the high local concentration of ions, produced *in situ* during synthesis, could induce the etching of mSiO$_2$ at this interface.

Since the etching mechanism of mSiO$_2$ shell could allow the PtPd metal core to expand, we sequentially reduced 10 batches of K$_2$PdCl$_4$ on Pt@mSiO$_2$ seeds to test how much the metal core can expand (Figure 2). Surprisingly, we obtained PtPd metal cores with an average size of 25.5 ± 3.0 nm after 10 growth cycles of Pd addition. Comparing to the original Pt core (12.4 ± 1.3 nm), the mSiO$_2$ shell is capable of accommodating an 8–fold volume expansion of the inner metal core. As more Pd deposited, it is also clearly seen that PtPd metal cores expand consistently and the mSiO$_2$ shell becomes thinner. More detailed mechanism studies about the changes in the mSiO$_2$ shell are underway. Nevertheless, the flexibility of mSiO$_2$ shell allows us to increase the metal core size without destroying the inorganic shell.

To show the versatility of our method, we demonstrated that monodisperse bimetallic NPs can be synthesized using mSiO$_2$ as the inorganic capping shell, when we used different metal precursors (H$_2$PtCl$_6$, K$_2$PtCl$_4$, Pd(acac)$_2$ and K$_2$PdCl$_4$), solvents (oleylamine and TEG), and reduction orders (Pd on Pt@mSiO$_2$ and Pt on Pd@mSiO$_2$). As summarized by (i)–(v) in Table 1, uniform PtPd@mSiO$_2$ NPs were formed regardless of diverse synthetic conditions. Even though bare PtPd NPs have been reported with spatial and structural controls via co– or sequential reduction of Pd or Pt precursors in polyol and/or oleylamine solvents, these synthetic methods are specifically dependent on a delicate choice of precursors, solvents, capping agents, temperatures, and reduction orders.[51-54] In the absence of the mSiO$_2$ shell encapsulation, under our synthetic conditions using TEG, we found that uniform PtPd NPs could hardly be synthesized by the direct deposition of Pd on Pt NPs. Even with the additional introduction of polyvinylpyrrolidone (PVP, Mw ~ 29000) as an organic capping agent to stabilize PtPd NPs in TEG, we still cannot synthesize uniform PtPd NPs (vi and vii, Table 1). Oleylamine was then inspected as a stronger capping agent than
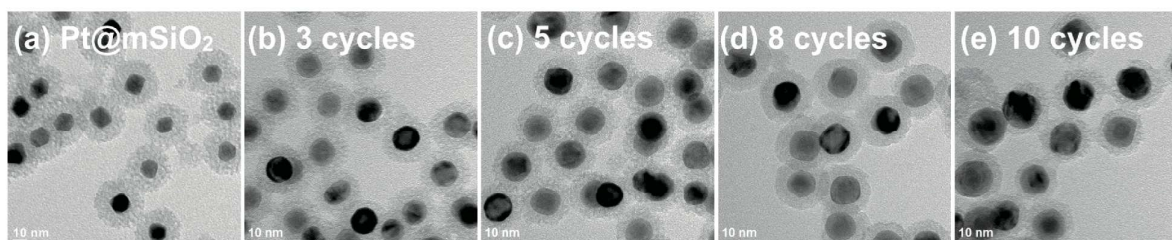
Nanoscale

ARTICLE

Figure 2. TEM images of PtPd$_x$@mSiO$_2$ after sequential addition of Pd to Pt@mSiO$_2$. The average sizes of (a) original Pt and PtPd metal core after (b) 3, (c) 5, (d) 8 and (e) 10 cycles of Pd addition are summarized as 12.4 ± 1.3 nm, 17.9 ± 1.1 nm, 20.2 ± 1.5 nm, 21.9 ± 2.2 nm and 25.5 ± 3.0 nm, respectively (based on 200 particles in each case). After each cycle of Pd addition, as–synthesized PtPd@mSiO$_2$ NPs were washed and redispersed as seeds for the next cycle.

Table 1. The effect of different synthetic conditions, including solvent, precursor, capping agent, and reduction order on the morphology of synthesized bimetallic NPs.

	Seed	Secondary metal	Solvent	Organic capping agent	Result	Reference
i.	Pt@mSiO$_2$	K$_2$PdCl$_4$	TEG	–	uniform PtPd@mSiO$_2$	Figure 1b
ii	Pt@mSiO$_2$	Pd(acac)$_2$	TEG	–	uniform PtPd@mSiO$_2$	Figure S3a
iii	Pd@mSiO$_2$	K$_2$PtCl$_4$	TEG	–	uniform PdPt@mSiO$_2$	Figure S4g
iv	Pd@mSiO$_2$	H$_2$PtCl$_6$	TEG	–	uniform PdPt@mSiO$_2$	Figure S3b
v	Pd@mSiO$_2$	H$_2$PtCl$_6$	Oleylamine	Oleylamine	uniform PtPd@mSiO$_2$	Figure S3c
vi	Pt NPs	K$_2$PdCl$_4$	TEG	—	chunks	Figure S3d
vii	Pt NPs	K$_2$PdCl$_4$	TEG	PVP	dispersive NPs	Figure S3e
viii	Pd NPs	H$_2$PtCl$_6$	Oleylamine	Oleylamine	flower–like Pd@Pt NPs	Figure S3f
ix	Pt NPs	Pd(acac)$_2$	Oleylamine	Oleylamine	isolated Pd clusters	Figure S3g

PVP, and flower–like Pd@Pt NPs with Pd clusters forming around Pt cores were attained as previously reported (viii, Table 1).[53] However, when we reversed the reduction order to deposit Pd(acac)$_2$ on Pt NPs, flower–like Pt@Pd NPs were not obtained, instead Pd nucleated independently of the available Pt seeds (ix, Table 1). These results demonstrate that the mSiO$_2$ shell is more robust as an inorganic stabilizer for seeded growth and renders our method less sensitive to synthetic conditions when accounting for other general organic capping agents.

To test the versatility of our method in regulating bimetallic compositions, we chose the PtPd@mSiO$_2$ system for detailed studies. By tuning the ratio of K$_2$PdCl$_4$ precursor to Pt@mSiO$_2$ seeds, various PtPd@mSiO$_2$ samples ranging from the Pt–rich to the Pd–rich region were synthesized, denoted as PtPd$_{0.50}$@mSiO$_2$,

PtPd$_{0.74}$@mSiO$_2$, PtPd$_{1.1}$@mSiO$_2$ and PtPd$_{1.6}$@mSiO$_2$. We also used Pd@mSiO$_2$ as seeds and reduced Pt precursor (K$_2$PtCl$_4$) on them under similar synthetic conditions as described for introducing the Pd precursor to Pt@mSiO$_2$. These bimetallic NPs prepared using Pd@mSiO$_2$ as seeds are denoted as PdPt$_{0.48}$@mSiO$_2$ and PdPt$_{1.1}$@mSiO$_2$. We utilized inductively coupled plasma mass spectroscopy (ICP–MS) to measure final Pd/Pt ratios. Measured Pd/Pt ratios agree well with those calculated from the starting materials (Table S3), which demonstrates the efficient incorporation of K$_2$PdCl$_4$ in bimetallic PtPd@mSiO$_2$ NPs. Additionally, the TEM images (Figure S4) show that no isolated metal NPs formed in all PtPd@mSiO$_2$ samples with various Pd/Pt ratios, even when 1.6 equivalents of Pd were introduced to Pt@mSiO$_2$. We also measured the average sizes of metal cores in

Pt@mSiO$_2$, PtPd$_{0.50}$@mSiO$_2$, PtPd$_{0.74}$@mSiO$_2$, PtPd$_{1.1}$@mSiO$_2$, and PtPd$_{1.6}$@mSiO$_2$ as 13.6 ± 1.0 nm, 15.5 ± 1.3 nm, 16.7 ± 1.2 nm, 17.7 ± 1.2 nm, and 19.1 ± 1.1 nm, respectively (Figure S5). Overall particle sizes (including the mSiO$_2$ shell) in all PtPd@mSiO$_2$ samples experienced no obvious change. The measured PtPd metal core sizes agree with the theoretical values assuming no Pt loss during the seeded growth (Figure 1d and Equation S1). Together with ICP–MS results in Table S3, it is evident that the robust confinement afforded by mSiO$_2$ ensured the successful introduction of Pd upon Pt@mSiO$_2$ seeds with tunable Pd/Pt ratios and high incorporation efficiency.
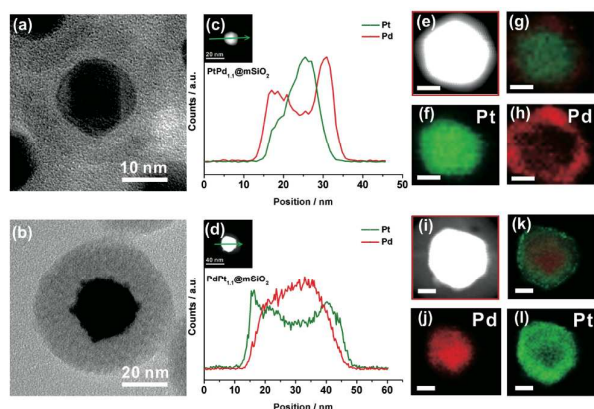

Figure 3. TEM images, EDS line scans, and elemental mappings: TEM images of the representative (a) as–synthesized PtPd$_{1.1}$@mSiO$_2$ NP to discern Pt core/Pd shell structure and (b) as–synthesized PdPt1.1@mSiO$_2$ NP with Pd core/Pt shell structure; EDS line scans of (c) PtPd$_{1.1}$@mSiO$_2$ and (d) PdPt1.1@mSiO2; e)–l) are elemental mapping images of Pt (green) and Pd (red) signals. The scale bars in e)–h) are all 5 nm, and in i)–l) are 10 nm.

The morphology of the PtPd metal core in as–synthesized PtPd@mSiO$_2$ was characterized by TEM coupled with energy dispersive X–ray spectroscopy (EDS) as shown in Figure 3 and Figure S6. The core–shell structure of the PtPd metal core can be observed in PtPd$_{1.1}$@mSiO$_2$ with the darker Pt core visualized within a lighter Pd shell (Figure 3a). After the deposition of Pd, the PtPd metal core in PtPd$_{1.1}$@mSiO$_2$ also illustrates a spherical shape, which differs from the more cubic–like Pt core in the original Pt@mSiO$_2$ seeds (Figure 1b and 1a). The Pt core/Pd shell structure in PtPd$_{1.1}$@mSiO$_2$ was further confirmed in Figure 3c and 3e–h under EDS line scan and elemental mapping. We observed Pt was localized in the inner position, while Pd was distributed around the Pt core as a ~ 5 nm shell. When we reversed the reduction order to form PdPt$_{1.1}$@mSiO$_2$ by introducing Pt on Pd@mSiO$_2$ seeds, a Pd core/Pt shell structure was also evident as expected (Figure 3b, 3d, and 3i–l). However, we could not exclude the deposition of secondary metal within the mSiO$_2$ network due to the limited sensitivity and resolution of EDS.

To further illustrate the core–shell structure, PdPt$_{0.48}$@mSiO$_2$ was obtained by coating the Pd core with a thin Pt shell, and placed in concentrated HNO$_3$ to engender the preferential chemical etching of Pd. Hollow Pt shell–like nanoboxes encapsulated in mSiO$_2$ were derived for the first time after etching away inner Pd cores in PdPt$_{0.48}$@mSiO$_2$ (Figure 1e). Starting with a Pd shell deposited on Pt@mSiO$_2$ core, we hypothesize that a Pt yolk–shell structure encapsulated in mSiO$_2$ (yolk–shell Pt@mSiO$_2$) can also be

acquired when removing the deposited Pd layer in between the original Pt core and the etched mSiO$_2$ shell. To prove this, we used HNO$_3$ to etch Pd in dried PtPd@mSiO$_2$ powders with a 21.9 nm PtPd core. As shown in Figure 1f, the metal cores decreased to ~ 13 nm, which is comparable to the original 12.4 nm Pt core, and the void space between the metal core and the mSiO$_2$ shell was clearly observed. Interestingly, if we directly etched Pd in as–synthesized PtPd@mSiO$_2$ without drying, we could not observe any yolk–shell structure (Figure S2e).[55] Based on these experiments, we envisage that the mSiO$_2$ shell can perform as a universal inorganic stabilizer enabling the synthesis of versatile nanostructures.

Under the protection of the mSiO$_2$ shell, PtPd@mSiO$_2$ experiences enhanced thermal stability, which facilitates the high–temperature treatment to convert the core–shell structure of PtPd metal cores into alloy phases. The high–temperature also helps remove organic remnants that could hinder the catalytic performance of PtPd metal cores. As–synthesized PtPd@mSiO$_2$ NPs were then calcined at 350 ˚C in air and reduced at 300 ˚C under 5% H$_2$/Ar flow. We then utilized powder X–ray diffraction (PXRD) to clarify the formation of PtPd alloy phases in PtPd@mSiO$_2$ after thermal treatment (Figure 4). The characteristic diffraction peaks (e.g. major peak around 39.7˚) in all PtPd@mSiO$_2$ samples after thermal treatment shift to higher diffraction angles towards Pd@mSiO$_2$ peak positions as the Pd/Pt ratio increases. Meanwhile, all characteristic diffraction peaks in pure Pt@mSiO$_2$ and Pd@mSiO$_2$ are aligned with that of the respective Pt and Pd bulk metal standards. This coherent trend of angle shift suggests the formation of PtPd alloy phases.[56] The formation of PtPd alloy phase is also confirmed with EDS line scan and elemental mapping (Figure S8). TEM images show that the mSiO$_2$ shell morphology was maintained and no aggregation of PtPd metal cores was observed in all PtPd@mSiO$_2$ samples after thermal treatment (the TEM image of PtPd$_{1.1}$@mSiO$_2$ annealed at 350˚C is shown in Figure S9h).
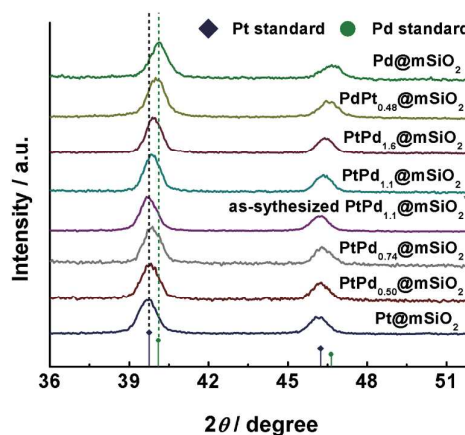

Figure 4. PXRD patterns of PtPd@mSiO$_2$ with various Pt/Pd ratios after calcination and reduction.

Nitrobenzene hydrogenation was used to evaluate the catalytic activity of PtPd@mSiO$_2$.[57] Since both Pt and Pd are hydrogenation catalysts, the total metal amount (Pt+Pd) was kept constant for all reaction studies.[58] For PtPd$_{1.1}$@mSiO$_2$ and PdPt$_{0.48}$@mSiO$_2$ catalysts (after annealing to form alloys), high conversion of nitrobenzene and high selectivity to aniline was obtained with less by–products

Nanoscale

ARTICLE

Table 2. Catalytic properties of PtPd@mSiO$_2$ and oleylamine–capped PtPd NPs in nitrobenzene hydrogenation.

Catalyst [a]	Conversion (%)	Capping agent	Yield (%) [b]			
			AN	NOB	AB	PHA
PdPt$_{0.50}$ NPs	61.1	oleylamine	19.8	3.9	5.4	32
PdPt$_{0.50}$/SiO$_2$	46.6	oleylamine	23.8	4.9	–	17.8
Pt$_{0.48}$Pd@mSiO$_2$	>99	mSiO$_2$	>99	–	–	–
PtPd$_{1.1}$@mSiO$_2$	90.2	mSiO$_2$	90.2	–	–	–

a. Catalysts experienced 350 ˚C calcination in air for 4 hrs and reduced at 300 ˚C under 5% H$_2$/Ar for 2 hrs before reaction except for PdPt$_{0.50}$ NPs; b. Aniline (AN), nitrosobenzene (NOB), azoxybenzene (AB) and phenylhydroxylamine (PHA) are four major products detected.

detected (Table 2). Notably, no obvious mSiO$_2$ shell destruction was observed after the reaction (Figure S10a). To further illustrate the difference in catalytic properties between mSiO$_2$–encapsulated PtPd NPs (PtPd@mSiO$_2$) prepared using this new inorganic capping strategy and general organic–stabilizer capped PtPd NPs, we investigated the catalytic performance of flower–like PdPt NPs synthesized in oleylamine for nitrobenzene hydrogenation (Table 2). When capped with oleylamine, PdPt NPs show decreased` conversion and poor selectivity in contrast to PtPd@mSiO$_2$. This suggests that oleylamine molecules may partially block surface active sites of metal NPs for the hydrogenation reaction. The oleylamine covered PdPt NP surface also complicates the product distribution likely due to the variation in electronic and steric characteristics of the metal surface. To help remove oleylamine from the metal surface, PdPt NPs were then loaded on silica gel and treated by calcination and reduction (PdPt/SiO$_2$). However, the conversion and selectivity of PdPt/SiO$_2$ were not improved and significant aggregation of the PtPd NPs were observed as shown in Figure S3h. Hence the mSiO$_2$ shell can promote the thermal stability of PtPd nanocatalysts with no distinct retardation to reactant/product diffusion for nitrobenzene hydrogenation. The reusability of PtPd@mSiO$_2$ was evaluated with high activity and selectivity achieved for 6 runs (Figure S11 and Table S4). We did observe that the mSiO$_2$ shell became thinner and partially damaged (Figure S10b) after 6 recycle runs, which could be due to the formation of the basic reaction product, aniline. Aniline could etch mSiO$_2$ over time and finally leaded to the aggregation of unprotected PtPd NPs and the decrease of their activity.

In order to extend this strategy to other bimetallic NPs of PtM@mSiO$_2$, Ni, Cu and Rh were introduced into Pt@mSiO$_2$ seeds to form PtNi@mSiO$_2$, PtCu@mSiO$_2$ and PtRh@mSiO$_2$, respectively. The molar ratios of the secondary metals to original Pt were measured by ICP–MS (Table S3). The compositions of as–synthesized PtM@mSiO$_2$ (M = Ni, Cu and Rh) revealed that the secondary metals have been successfully introduced into Pt@mSiO$_2$. From Figure S9a–c, the diameter increase in the metal core and the preserved mSiO$_2$ shell after introducing the secondary metals confirm the induced growth of additive metal precursors on Pt@mSiO$_2$ seeds. The elemental mappings and EDS line scans of PtNi@mSiO$_2$ and PtRh@mSiO$_2$ also suggest the successful introduction of secondary metals (Figure S12 and S13). We thereupon applied high–temperature annealing to induce alloy phases as confirmed by PXRD patterns of PtM@mSiO$_2$ before and after annealing in Figure S14. All PtM@mSiO$_2$ after annealing clearly show consistent peak shifts to higher diffraction angles with peak positions in between Pt and corresponding secondary bulk metal standards. In addition, mSiO$_2$ shells in all PtM@mSiO$_2$ NPs were retained after annealing with no aggregation of metal NPs being observed (Figure S9e–g).

Conclusions

In summary, we have demonstrated the versatility of the inorganic capping strategy in the seeded growth of various bimetallic PtM@mSiO$_2$ NPs. Unique structures (core–shell, alloy, box, and yolk–shell) were synthesized using this strategy starting from Pt@mSiO$_2$ or Pd@mSiO$_2$ seeds. With the assistance of the mSiO$_2$ shell as an inorganic stabilizer, our method provides tunability in bimetallic composition and structure, promoted thermal stability, as well as desirable size control of bimetallic NPs. We believe that this synthetic route can be extended to the synthesis of a broad spectrum of alloy and intermetallic nanostructures for structural and catalytic studies.

Acknowledgements

Nanoscale Accepted Manuscript

ARTICLE

Notes and references

1. R. Han, J. W. Ha, C. Xiao, Y. Pei, Z. Qi, B. Dong, N. L. Bormann, W. Huang and N. Fang, *Angew. Chem. Int. Ed.*, 2014, **53**, 12865–12869.
2. H. Wang, W. Zhou, J. X. Liu, R. Si, G. Sun, M. Q. Zhong, H. Y. Su, H. B. Zhao, J. A. Rodriguez, S. J. Pennycook, J. C. Idrobo, W. X. Li, Y. Kou and D. Ma, *J. Am. Chem. Soc.*, 2013, **135**, 4149–4158.
3. C. Xiao, R. V. Maligal–Ganesh, T. Li, Z. Qi, Z. Guo, K. T. Brashler, S. Goes, X. Li, T. W. Goh, R. E. Winans and W. Huang, *ChemSusChem*, 2013, **6**, 1915–1922.
4. S. Zhang, Y. Hao, D. Su, V. V. Doan–Nguyen, Y. Wu, J. Li, S. Sun and C. B. Murray, *J. Am. Chem. Soc.*, 2014, **136**, 15921–15924.
5. X. Huang, Y. Li, Y. Li, H. Zhou, X. Duan and Y. Huang, *Nano Lett.*, 2012, **12**, 4265–4270.
6. Y. Liu, H. Tsunoyama, T. Akita, S. Xie and T. Tsukuda, *ACS Catal.*, 2011, **1**, 2–6.
7. F. Tao, M. E. Grass, Y. Zhang, D. R. Butcher, J. R. Renzas, Z. Liu, J. Y. Chung, B. S. Mun, M. Salmeron and G. A. Somorjai, *Science*, 2008, **322**, 932–934.
8. C. Chen, Y. Kang, Z. Huo, Z. Zhu, W. Huang, H. L. Xin, J. D. Snyder, D. Li, J. A. Herron, M. Mavrikakis, M. Chi, K. L. More, Y. Li, N. M. Markovic, G. A. Somorjai, P. Yang and V. R. Stamenkovic, *Science*, 2014, **343**, 1339–1343.
9. B. T. Sneed, C. N. Brodsky, C. H. Kuo, L. K. Lamontagne, Y. Jiang, Y. Wang, F. F. Tao, W. Huang and C. K. Tsung, *J. Am. Chem. Soc.*, 2013, **135**, 14691–14700.
10. L. Wang and Y. Yamauchi, *J. Am. Chem. Soc.*, 2013, **135**, 16762–16765.
11. L. R. Alden, C. Roychowdhury, F. Matsumoto, D. K. Han, V. B. Zeldovich, H. D. Abruña and F. J. DiSalvo, *Langmuir*, 2006, **22**, 10465–10471.
12. S. I. Sanchez, M. W. Small, J.–M. Zuo and R. J. Nuzzo, *J. Am. Chem. Soc.*, 2009, **131**, 8683–8689.
13. A. Meffre, B. Mehdaoui, V. Connord, J. Carrey, P. F. Fazzini, S. Lachaize, M. Respaud and B. Chaudret, *Nano Lett.*, 2015, DOI: 10.1021/acs.nanolett.5b00446.
14. S. Alayoglu, A. U. Nilekar, M. Mavrikakis and B. Eichhorn, *Nat. Mater.*, 2008, **7**, 333–338.
15. H. Lee, S. E. Habas, G. A. Somorjai and P. Yang, *J. Am. Chem. Soc.*, 2008, **130**, 5406–5407.
16. S. E. Habas, H. Lee, V. Radmilovic, G. A. Somorjai and P. Yang, *Nat. Mater.*, 2007, **6**, 692–697.
17. Z. Wang, Z. Chen, H. Zhang, Z. Zhang, H. Wu, M. Jin, C. Wu, D. Yang and Y. Yin, *ACS Nano*, 2015, **9**, 3307–3313.
18. C.–K. Tsung, J. N. Kuhn, W. Huang, C. Aliaga, L.–I. Hung, G. A. Somorjai and P. Yang, *J. Am. Chem. Soc.*, 2009, **131**, 5816–5822.
19. S. Alayoglu and B. Eichhorn, *J. Am. Chem. Soc.*, 2008, **130**, 17479–17486.
20. S. G. Kwon, G. Krylova, A. Sumer, M. M. Schwartz, E. E. Bunel, C. L. Marshall, S. Chattopadhyay, B. Lee, J. Jellinek and E. V. Shevchenko, *Nano Lett.*, 2012, **12**, 5382–5388.
21. Y. Xia, Y. Xiong, B. Lim and S. E. Skrabalak, *Angew. Chem. Int. Ed.*, 2009, **48**, 60–103.
22. Z. Niu and Y. Li, *Chem. Mater.*, 2014, **26**, 72–83.
23. J. A. Lopez–Sanchez, N. Dimitratos, C. Hammond, G. L. Brett, L. Kesavan, S. White, P. Miedziak, R. Tiruvalam, R. L. Jenkins, A. F. Carley, D. Knight, C. J. Kiely and G. J. Hutchings, *Nat. Chem.*, 2011, **3**, 551–556.
24. S. F. J. Hackett, R. M. Brydson, M. H. Gass, I. Harvey, A. D. Newman, K. Wilson and A. F. Lee, *Angew. Chem. Int. Ed.*, 2007, **119**, 8747–8750.
25. K. An, S. Alayoglu, N. Musselwhite, S. Plamthottam, G. Melaet, A. E. Lindeman and G. A. Somorjai, *J. Am. Chem. Soc.*, 2013, **135**, 16689–16696.
26. Y. Gao, D. Ma, C. Wang, J. Guan and X. Bao, *Chem. Commun.*, 2011, **47**, 2432–2434.
27. R. M. Rioux, H. Song, J. D. Hoefelmeyer, P. Yang and G. A. Somorjai, *J. Phys. Chem. B*, 2005, **195**, 2192–2202.
28. H. Zhu, A. Sigdel, S. Zhang, D. Su, Z. Xi, Q. Li and S. Sun, *Angew. Chem. Int. Ed.*, 2014, **53**, 12508–12512.
29. W. Zhang, Z. X. Chi, W. X. Mao, R. W. Lv, A. M. Cao and L. J. Wan, *Angew. Chem. Int. Ed.*, 2014, **53**, 12776–12780.
30. T. Zhang, H. Zhao, S. He, K. Liu, H. Liu, Y. Yin and C. Gao, *ACS Nano*, 2014, **8**, 7297–7304.
31. C. Nan, Z. Lin, H. Liao, M. K. Song, Y. Li and E. J. Cairns, *J. Am. Chem. Soc.*, 2014, **136**, 4659–4663.
32. J. Mielby, J. O. Abildstrom, F. Wang, T. Kasama, C. Weidenthaler and S. Kegnaes, *Angew. Chem. Int. Ed.*, 2014, **53**, 12513–12516.
33. X. Li, X. Wang, D. Liu, S. Song and H. Zhang, *Chem. Commun.*, 2014, **50**, 7198–7201.
34. J. B. Joo, I. Lee, M. Dahl, G. D. Moon, F. Zaera and Y. Yin, *Adv. Funct. Mater.*, 2013, **23**, 4246–4254.
35. W. Li, J. Yang, Z. Wu, J. Wang, B. Li, S. Feng, Y. Deng, F. Zhang and D. Zhao, *J. Am. Chem. Soc.*, 2012, **134**, 11864–11867.
36. C. Chen, X. Fang, B. Wu, L. Huang and N. Zheng, *ChemCatChem*, 2012, **4**, 1578–1586.
37. B. Guo, X. Wang, P. F. Fulvio, M. Chi, S. M. Mahurin, X. G. Sun and S. Dai, *Adv. Mater.*, 2011, **23**, 4661–4666.
38. H.–P. Zhou, H.–S. Wu, J. Shen, A.–X. Yin, L.–D. Sun and C.–H. Yan, *J. Am. Chem. Soc.*, 2010, **132**, 4998–4999.
39. C. J. Zhong and M. M. Maye, *Adv. Mater.*, 2001, **13**, 1507–1511.
40. L. M. Liz–Marzán, M. Giersig and P. Mulvaney, *Langmuir*, 1996, **12**, 4329–4335.
41. X. Li, L. Zhou, Y. Wei, A. M. El–Toni, F. Zhang and D. Zhao, *J. Am. Chem. Soc.*, 2015, DOI: 10.1021/jacs.5b03207.
42. S. H. Joo, J. Y. Park, C. K. Tsung, Y. Yamada, P. Yang and G. A. Somorjai, *Nat. Mater.*, 2009, **8**, 126–131.
43. H. Liu, H. Yu, C. Xiong and S. Zhou, *RSC Adv.*, 2015, **5**, 20238–20247.
44. S. Zhao, Y. Chen and Z. Liu, *RSC Adv.*, 2015, **5**, 33299–33305.
45. J. C. Bauer, X. Chen, Q. Liu, T.–H. Phan and R. E. Schaak, *J. Mater. Chem.*, 2008, **18**, 275–282.
46. N. T. Thanh, N. Maclean and S. Mahiddine, *Chem. Rev.*, 2014, **114**, 7610–7630.
47. M. Salciccioli and D. G. Vlachos, *J Phys Chem A*, 2012, **116**, 4621–4628.
48. C. Bock, C. Paquet, M. Couillard, G. A. Botton and B. R. MacDougal, *J. Am. Chem. Soc.*, 2004, **126**, 8028–8037.
49. S. E. Skrabalak, B. J. Wiley, M. Kim, E. V. Formo and Y. Xia, *Nano Lett.*, 2008, **8**, 2077–2081.
50. J. P. Icenhower and P. M. Dove, *Geochim. Cosmochim. Acta.*, 2000, **64**, 4193–4203.

Nanoscale Accepted Manuscript

51. P. Zhang, Y. Hu, B. Li, Q. Zhang, C. Zhou, H. Yu, X. Zhang, L. Chen, B. Eichhorn and S. Zhou, *ACS Catal.*, 2015, **5**, 1335–1343.

52. S. Xie, S. I. Choi, N. Lu, L. T. Roling, J. A. Herron, L. Zhang, J. Park, J. Wang, M. J. Kim, Z. Xie, M. Mavrikakis and Y. Xia, *Nano Lett.*, 2014, **14**, 3570–3576.

53. N. Ortiz, R. G. Weiner and S. E. Skrabalak, *ACS Nano*, 2014, **8**, 12461–12467.

54. S. Khanal, G. Casillas, J. J. Velazquez–Salazar, A. Ponce and M. Jose–Yacaman, *J. Phys. Chem. C* 2012, **116**, 23596–23602.

55. M. Lin, Y. Wang, X. Sun, W. Wang and L. Chen, *ACS Appl. Mater. Interfaces*, 2015, **7**, 7516–7525.

56. Y.–F. Han, D. Kumar, C. Sivadinarayana, A. Clearfield and D. W. Goodman, *Catal. Lett.*, 2004, **94**, 3–4.

57. A. Corma and P. Serna, *Science*, 2006, **313**, 332–334.

58. A. Corma, P. Concepción and P. Serna, *Angew. Chem.*, 2007, **119**, 7404–7407.